Electronic Supplementary Material (ESI) for Journal of Materials Chemistry C.

Environmentally Phase-control Stratagem for Pyrophosphate Anode Material in Battery Energy Storage

Jianyong Zhang[1], Jiafeng Zhang[2,*], Jun Liu [2,*], Yang Cao[3], Xing Ou[3], Cancan Huang[3], Guanjun Ji[3], Zaowen Zhao[3], Bao Zhang[3]

[1]*National Engineering Laboratory for High Efficiency Recovery of Refractory Nonferrous Metals, School of Metallurgy and Environment, Central South University, Changsha 410000, PR China*

[2]*Department of Radiology, the Second Xiangya Hospital of Central South University, Changsha 410000, PR China*

[3]*Medical Engineering Center, Xiangya Hospital of Central South University, Changsha 410008, P.R. China.*

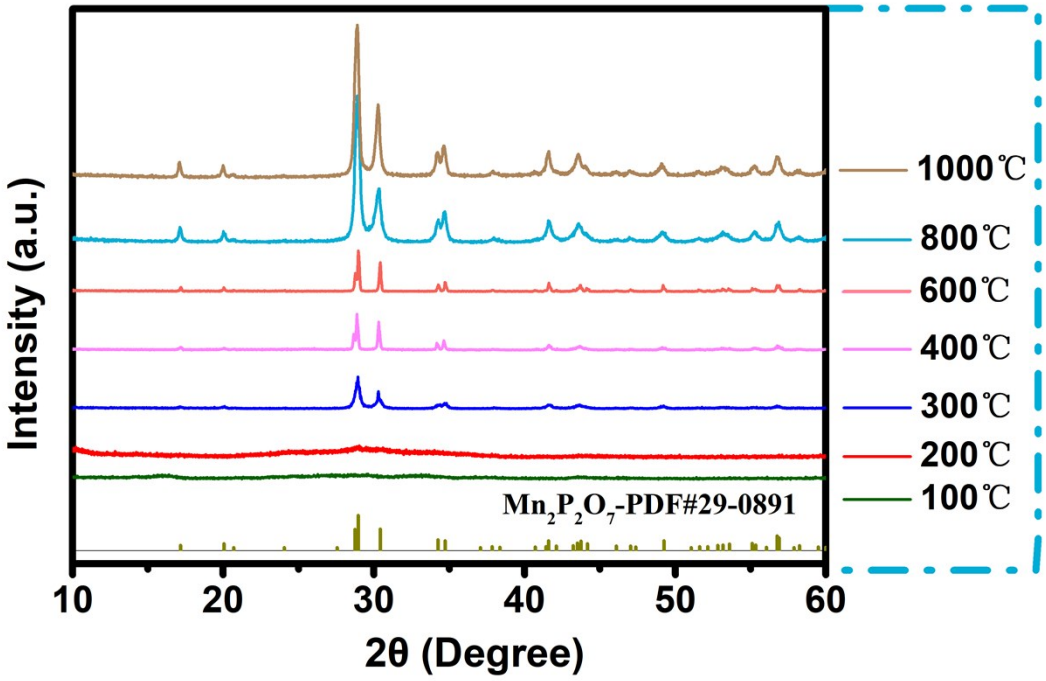

Fig. S1. Sintering temperature gradient of MPO.

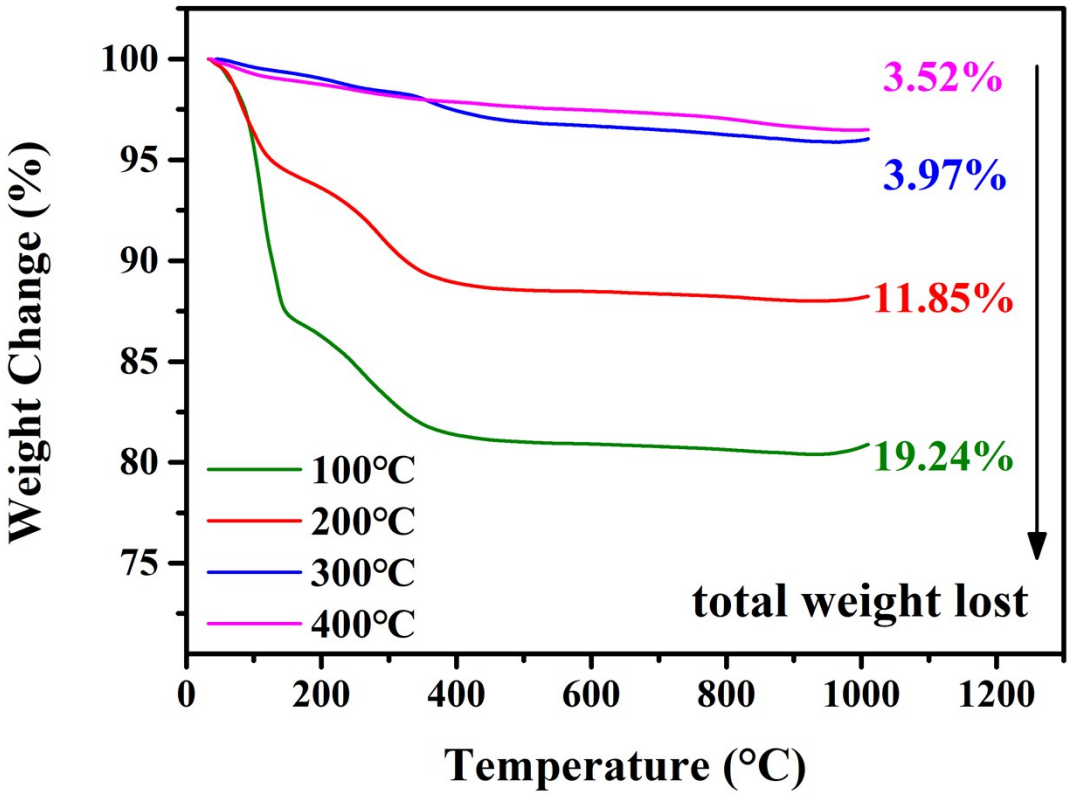

Fig. S 2. TG of 100-400 ℃ of MPO.

The samples are sintering at gradient of temperature from 100 ℃-1000 ℃ labeled as MPO-100, MPO- 200, MPO-300, MPO-400, MPO- 600, MPO-800, MPO-1000, and further investigated via TG-DTA. As we can see from Fig. S2, after sintering at different temperature. The sintering process is aimed to remove the few water and tiny organic residual in the sample.The MPO-100 and MPO- 200 samples show a huge weight lost before 200 ℃, which is due to the absorb surface water, and the sample show second weight lost around 200 ℃~300 ℃, which is due to the organic solution lost (ethanol). Hence, MPO-300, MPO- 400 sample mirror less weight lost, which is accordance with this. As a result, MPO-300, is chose for best sample with consideration of low energy cost and high crystal structure. The detail and refined crystal structure and XRD refine pattern are show in Fig. S4. The Rietveld refined XRD result shows Rwp=10.83%, Rwp=10.11% for MPO (Fig. S4) and MPO-rGO (Fig. 3a), which is satisfied with refinement result.

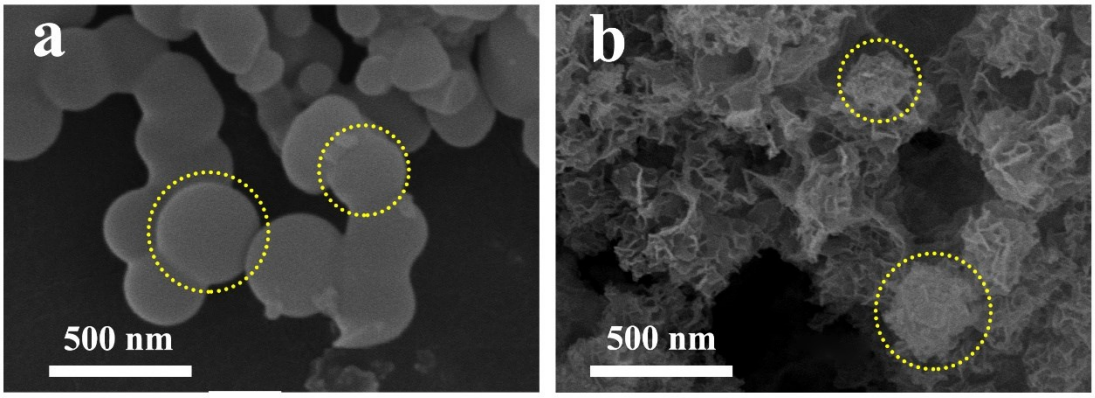

Fig. S 3. SEM of MPO and MPO-rGO.

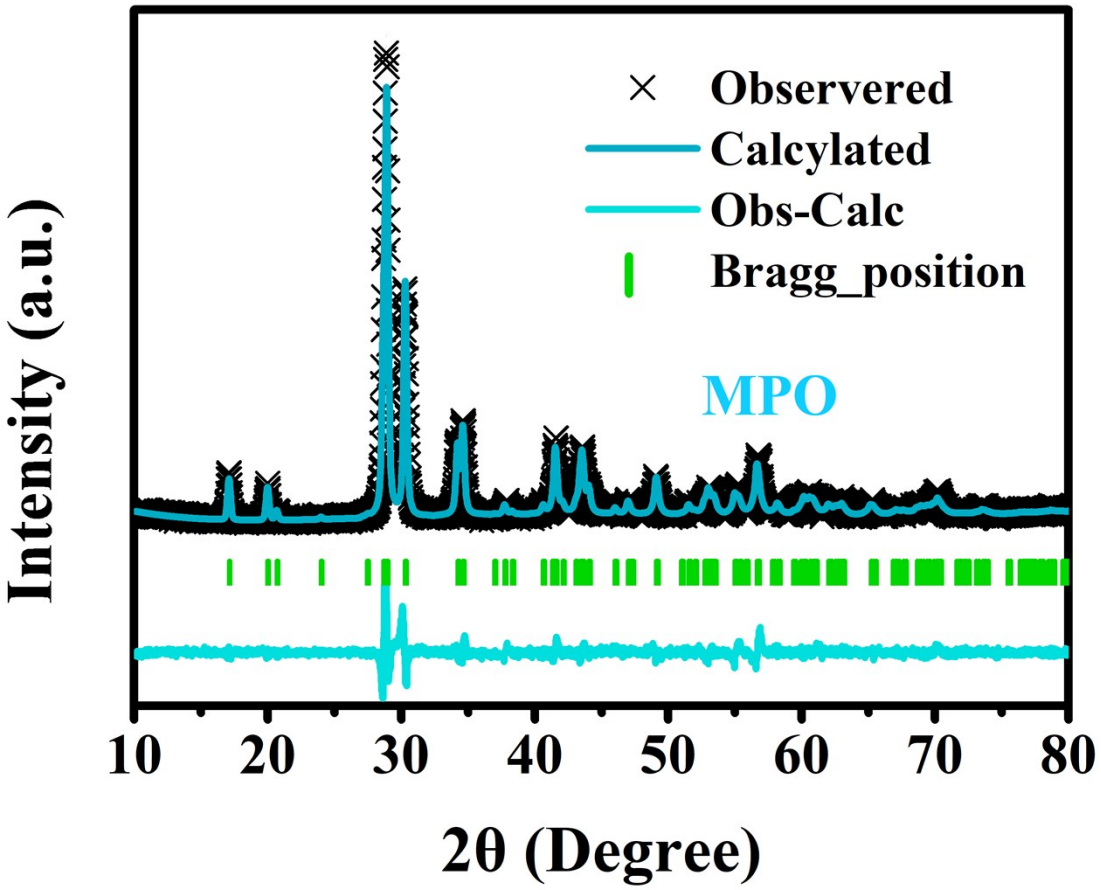

Fig. S 4. XRD diffraction pattern of the MPO

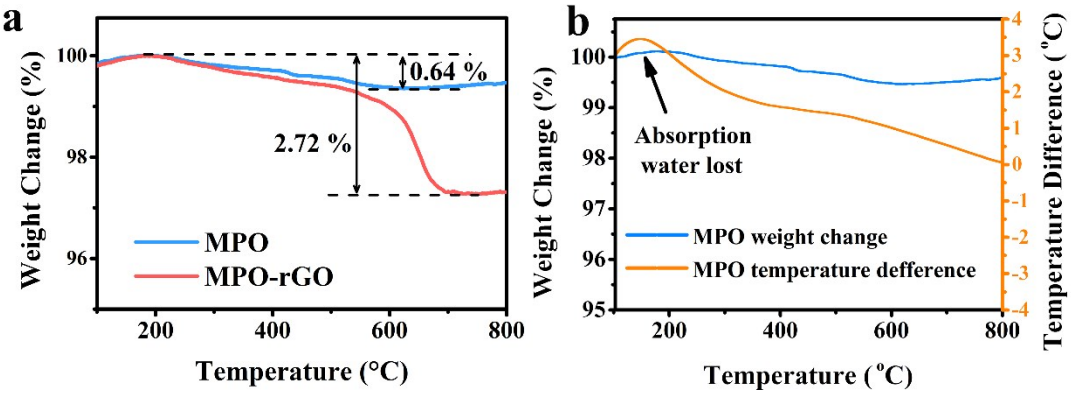

Fig. S 5. (a) The TGA curve and (b) DTG curve of MPO and MPO-rGO samples.

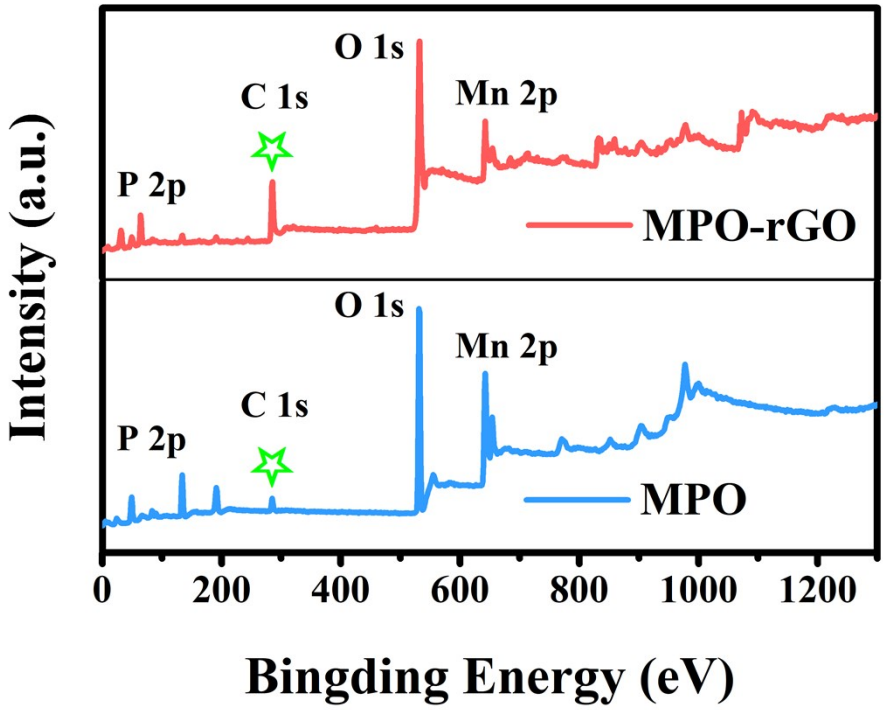

Fig. S 6. XPS curve of MPO and MPO-rGO.

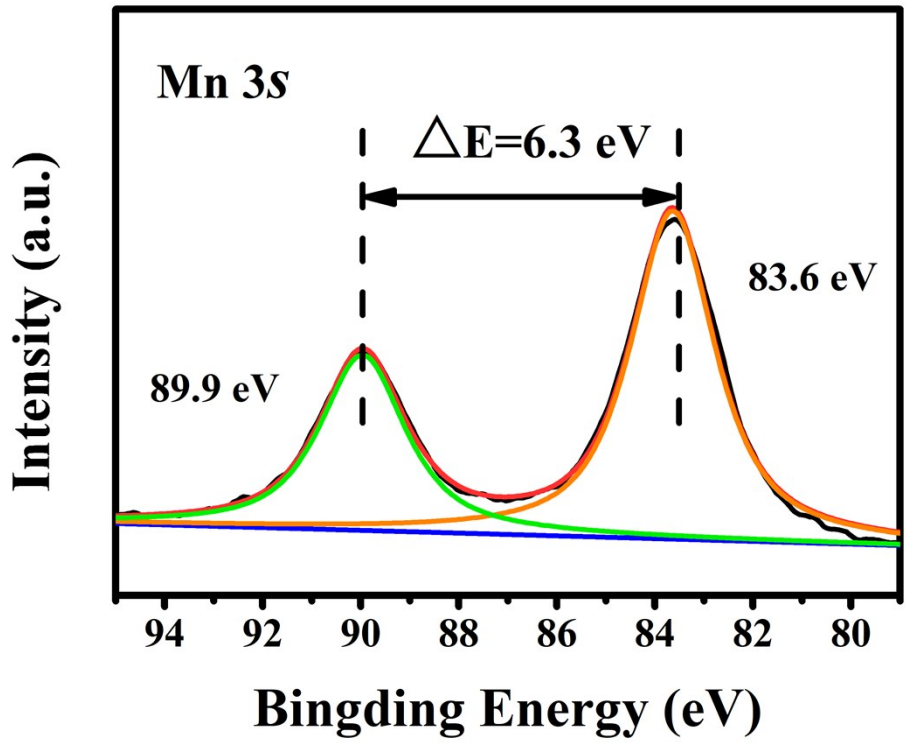

Fig. S 7. XPS pattern of Mn 3s.

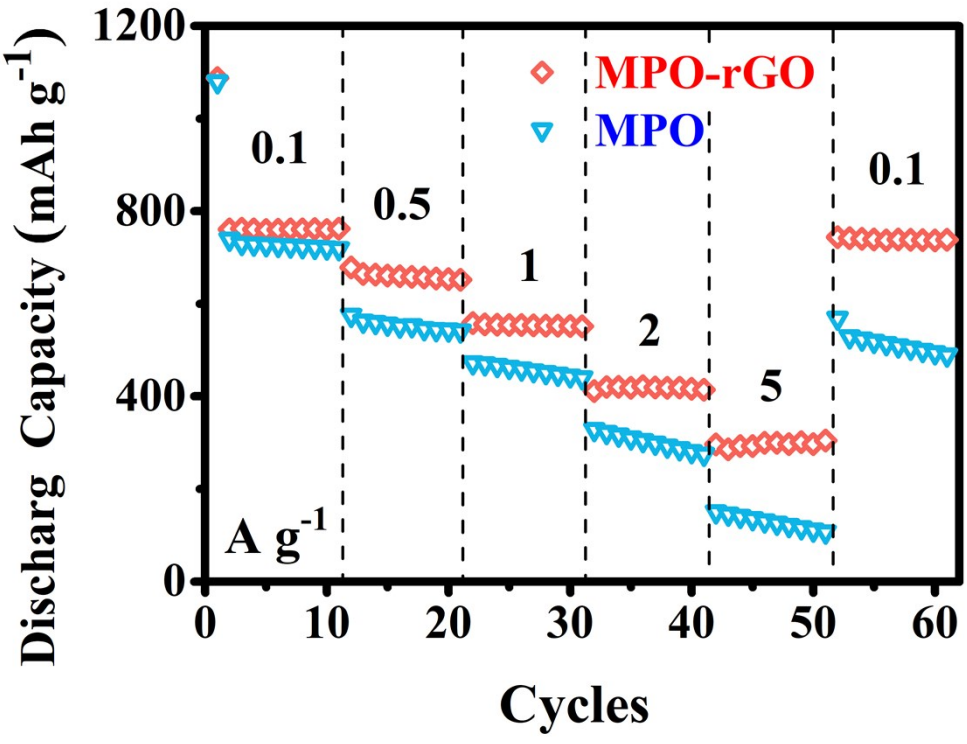

Fig. S 8. Rate performance of MPO and MPO-rGO.

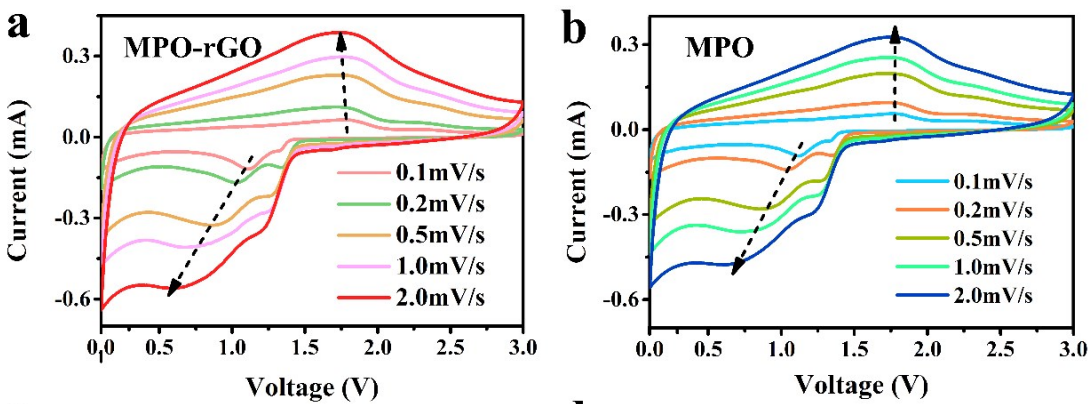

Fig. S 9. (a, b) Series scan of CV curve of MPO and MPO-rGO samples.

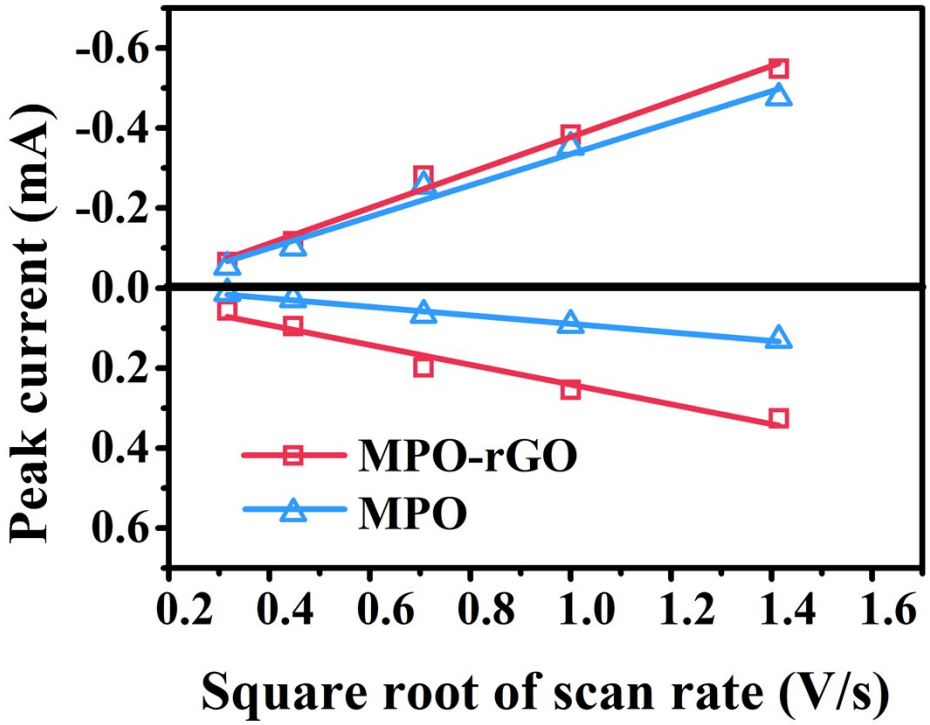

Fig. S 10. lithium ion diffusion rate.

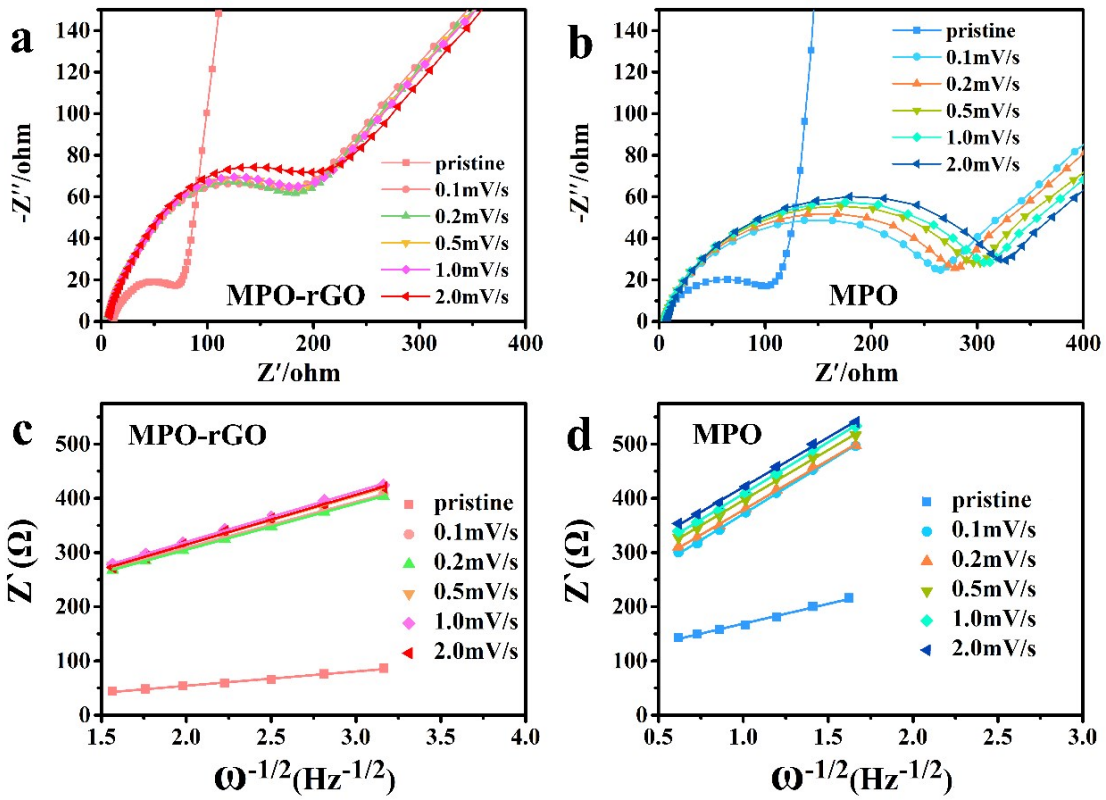

Fig. S 11. Lithium ion diffusion factor after cycled that calculated based EIS curve.

Fig. S 12. The model in equivalent circuit based on the Nyquist plots.

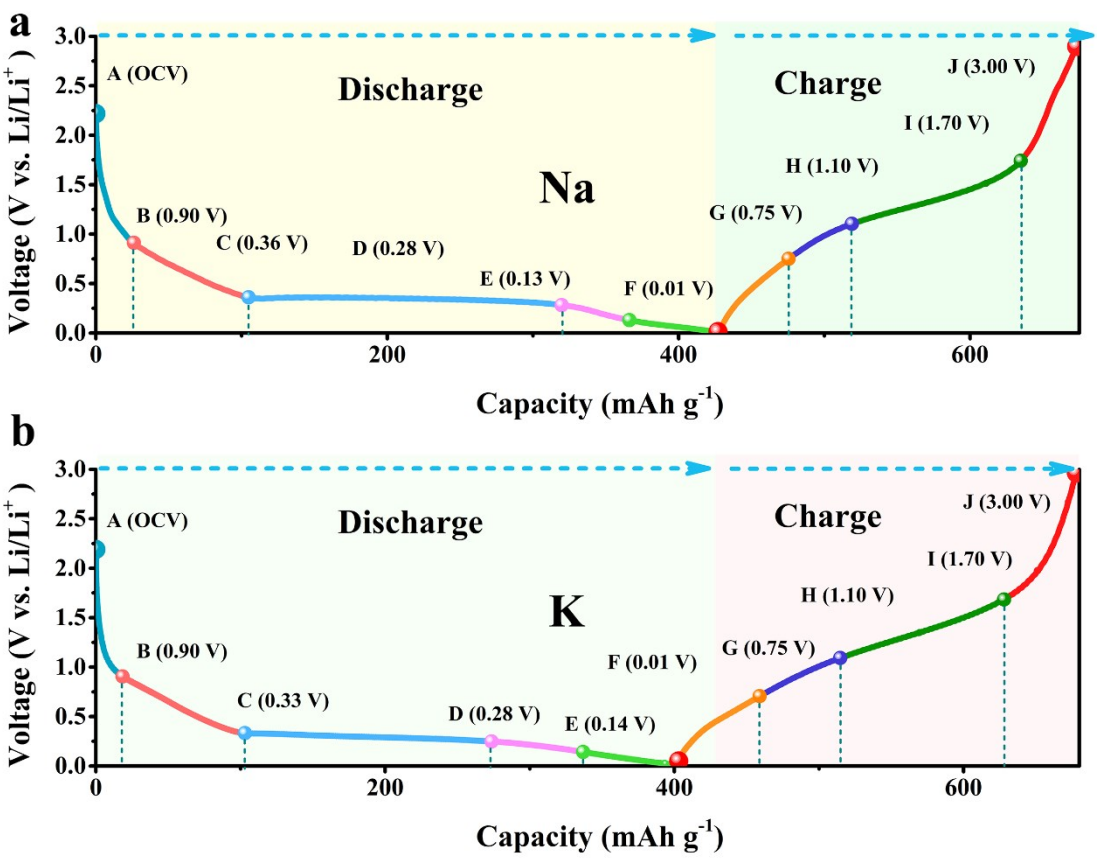

Fig. S 13. (a) Discharge/ Charge curve of sodium ion battery system, (b) Discharge/ Charge curve of potassium ion battery system

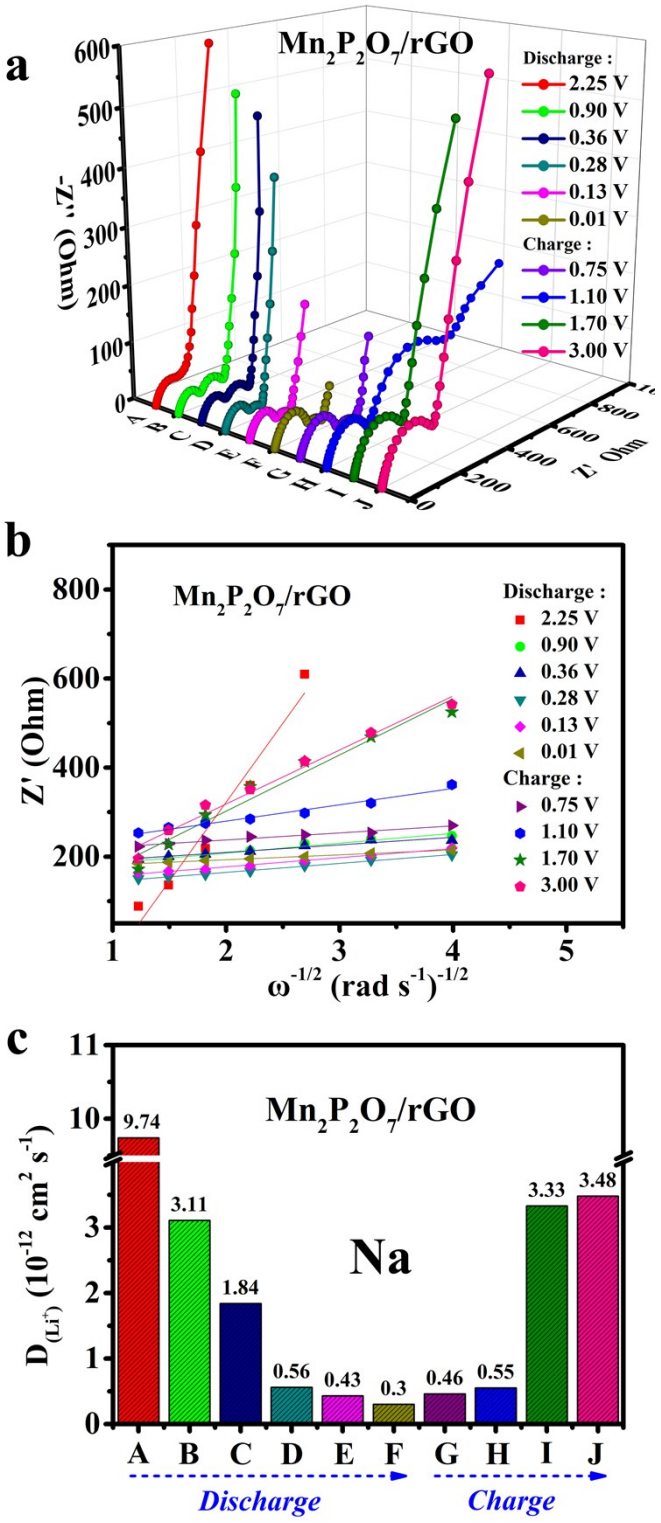

Fig. S 14. (a) In-suit EIS curve of MPO-rGO materials in sodium ion batteris. (b) Relationship of Z` and $\omega^{-1/2}$ plot. (c) Lithium ion diffusion rate of MPO-rGO materials in SIBs.

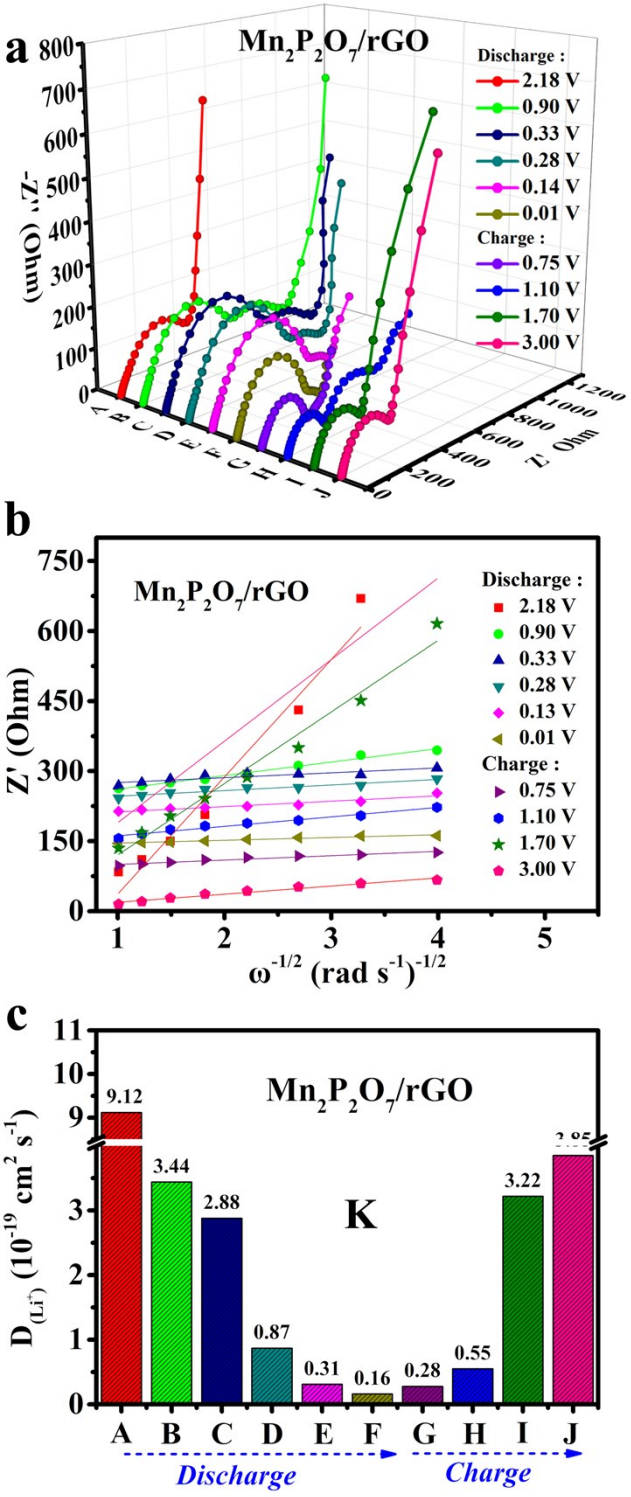

Fig. S 15. (a) In-suit EIS curve of MPO-rGO materials in potassium ion batteris (PIBs). (b) Relationship of Z` and $\omega^{-1/2}$ plot. (c) Lithium ion diffusion rate of MPO-rGO materials in PIBs.

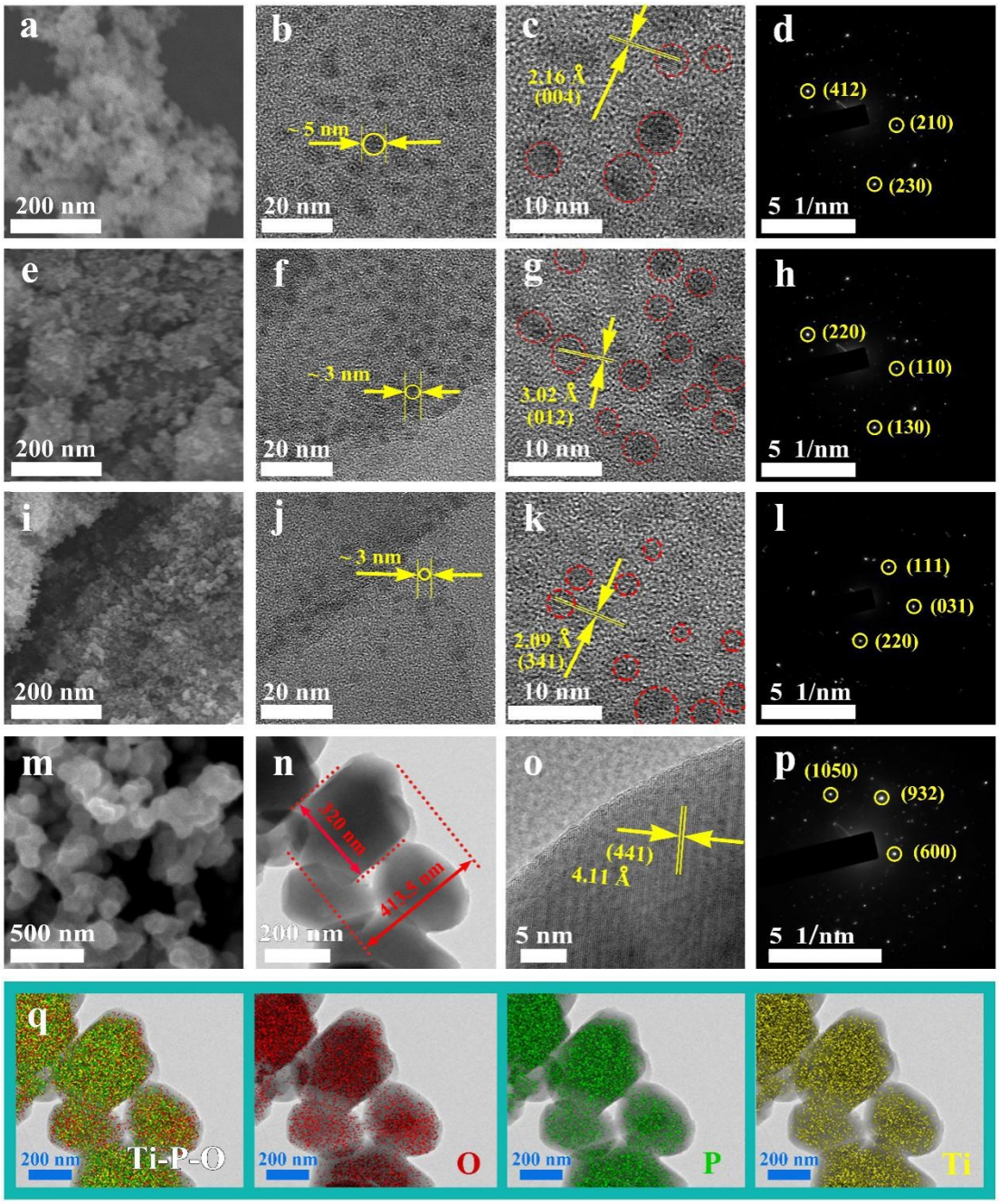

Fig. S. 16. SEM (a) and HRTEM (b, c) and SEAD (d) of $Ni_2P_2O_7$ material. SEM (e) and HRTEM (f, g) and SEAD (h) of $Co_2P_2O_7$ material. SEM (i) and HRTEM (j,k) and SEAD (l) of $Fe_2Fe(P_2O_7)_2$ material. SEM (m) and HRTEM (n, o) and SEAD (p) and mapping (q) of TiP_2O_7 material.

Morphologies of four types of $Co_2P_2O_7$, $Ni_2P_2O_7$, TiP_2O_7, $Fe_2Fe(P_2O_7)_2$ are indexed via TEM and SEM. Fig. S16a displays morphology of $Ni_2P_2O_7$ which assigns

to small grains in SEM image. The particles of $Ni_2P_2O_7$ are around 5 nm under HRTEM test in Fig. S16b, which is matched with lattice pattern as 2.16 Å in Fig. S16c. Meanwhile, SEAD test is further proofing that material is corresponding with $Ni_2P_2O_7$ with the marked spots (Fig. S16d) as (412), (210), (230). Additionally, $Co_2P_2O_7$ (Fig. S16e) and $Fe_2Fe(P_2O_7)_2$ (Fig. S16i) present similar morphology as nano particle, which both index about 3 nm in HRTEM image of Fig. S16f and Fig. S16j. Besides, lattice fringe for $Co_2P_2O_7$ and $Fe_2Fe(P_2O_7)_2$ materials are displayed as 3.02 Å (Fig. S16g) and 2.09 Å (Fig. S16k) respectively. Furthermore, The SEAM of $Co_2P_2O_7$ and $Fe_2Fe(P_2O_7)_2$ are provided in Fig. S16h and Fig. S16l, matching with marked spots of (220), (110), (130) and (111), (031), (220). Microparticle of TiP_2O_7 material is displayed in Fig. S16m, which obviously shows size of a small particle is around 413.5 nm in length and 320 nm in width. Crystal structure property of TiP_2O_7 material in Fig. S16n. Lattice plane is assigned to lattice spacing of 0.411 nm (441) in (Fig. S16o). Meanwhile, SEAD (Fig. S16p) of this sample is in accordance with series spots marked as (600), (932), (1050), which further verifies that sample is qualified with pure phase TiP_2O_7. Additionally, mapping test is applied to measure the dispersion of element in structure. As we can see in Fig. S16q, the combined mapping of Ti-P-O image shows uniform composed, and individual P and Ti, O element are homogeneously dispersed on particle, which illustrates that TiP_2O_7 material is successfully fabricated with uniform phase.

All morphologies of these four kinds of materials are identified as pure phase of PPM which further verified that this novel method possesses abundance application to a wide range of phase-control synthesis. Moreover, it might provide more inspiration to new material synthesis to Li-ion battery.

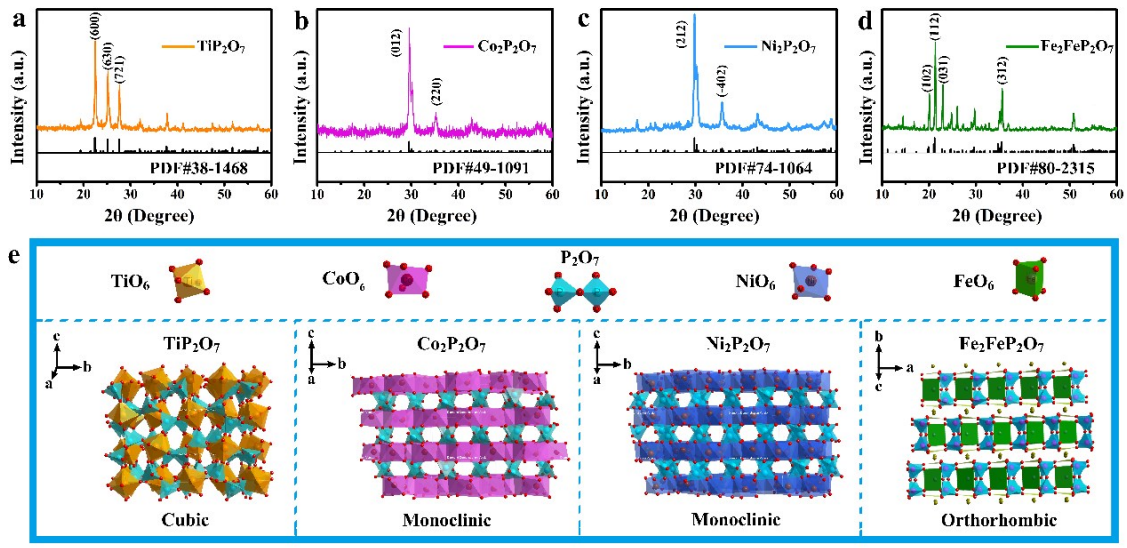

Fig. S17. XRD pattern of TiP_2O_7 (a), $Ni_2P_2O_7$ (b), $Co_2P_2O_7$ (c), $Fe_2Fe(P_2O_7)_2$ (d). (e) Crystal structure of four PPM aforementioned.

The XRD patterns of obtained materials are shown in Fig. S17. All samples possess clear X-ray diffraction peaks which mean precipitation method leading to good pyrophosphate crystalline structure. Fig. S17a displays X-ray diffraction curve of TiP_2O_7 that is matched well with the standard PDF card of PDF#38-1468, suggesting that the material is belong to space group of Pa3 (205), Three main peaks appear at angle of 22.55° (600), 25.25° (630), 27.70° (721), which is in agreement with pure phase PPM as previous works reported.

As shown in Fig. S17b and Fig. S17c, peaks of two curves are corresponding with standard PDF of $Ni_2P_2O_7$ (PDF#74-1604) and $Co_2P_2O_7$ (PDF#49-1091), meaning material is of consistency with pure phase of PPM. Interestingly, as obtained $Ni_2P_2O_7$ and $Co_2P_2O_7$ deliver similar space group which both belong to the B21/c (14) space group and both attribute to monoclinic system as presented in Fig. S17e. This means that we can obtain same type of PPMs by changing similar meatal ion (Ni, Co) bonding with PA, such as manganese ion. The same crystal structure means that this novel method is of potential to synthesize a group of PPMs, only if we shift similar metal ion to react with PA. To verify this, we successfully obtain the $Mn_2P_2O_7$ material via this method which is in accordance with space group of monoclinic and standard card pf PDF shown in Fig. S17. This result suggests that precipitation method qualifies

potential for fabricating more kinds of pyrophosphate materials as energy storage material. Fig. S17b presents two split main peaks of $Ni_2P_2O_7$ at angel of 29.82°, and 30.36° corresponding with peaks of (212) and (-402). Meanwhile, $Co_2P_2O_7$ X-ray diffraction cure shows similar with two main split peaks at 29.54° (012), 30.05° (-302).

Herein, we innovatively obtain stable and pure phase $Fe_2Fe(P_2O_7)_2$ material by precipitation method, and apply it into anode material for Li-ion battery. From X-ray diffraction (XRD) pattern in Fig. S17d, we can see that all peaks are in agreement with the pattern of orthorhombic $Fe_2Fe(P_2O_7)_2$ (PDF#80-2315), and multiple peaks appear around 20.06° (102), 21.34° (112), 23.48° (031), 35.66° (312), which belong to the pure phase of $Fe_2Fe(P_2O_7)_2$. The crystal details are delivered in Fig. S17e, according with orthorhombic system.

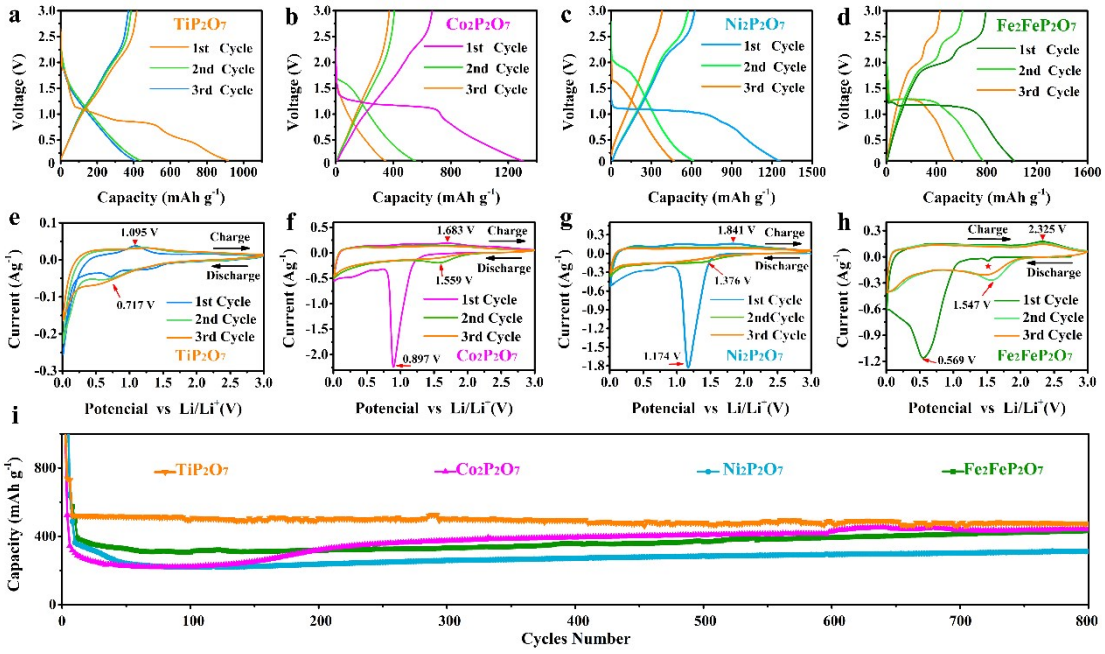

Fig. S18. (a, b, c, d) Charge and discharge plots in 0.1 A g^{-1} and (e, f, g, h) CV curve of MP_2O_7 material (M=Ti, Co, Ni, Fe). (i) Electrochemical performance of TiP_2O_7, $Ni_2P_2O_7$ and $Co_2P_2O_7$, $Fe_2Fe(P_2O_7)_2$ material in 0.5 A g^{-1}.

To further understand electrochemical process, discharge/charge plot of TiP_2O_7 shows in Fig. S18a, illustrating the 1st to 3rd cycling characteristics with voltage of 0.01-3.00 V. The first cycling plot presents voltage platform around 0.700 V during discharge process and delivers a slight voltage platform about 1.000 V for charge process. Meanwhile, 2nd and 3rd cycles present close discharge/charge behavior with

retention rate for 99.5% and 99.1%, showing stable electrochemical performance. For first anodic reaction in CV curves in Fig. S18e, an obvious peak appears at specific voltage of 0.717 V which is associated with transformation reaction in equation (eq) (1). For cathodic reaction, a peak refers to 1.095 V relating to chemical reaction in eq (2). Obviously, discharge/charge results are corresponding with CV measurement of TiP_2O_7. Electrochemical reactions of TiP_2O_7 material are only related to two-phase reaction, attributing to the conversion efficiency limitation of Ti^{4+} and Ti^{3+}. Furthermore, anodic and cathodic peaks intensity become weak from 1st cycle to 2nd and 3rd cycles which probably attributes to incomplete lithium conversion rate (x). where x showing in both anodic and cathodic reaction function in eq (1) and eq (2) is less than 1 for insufficient lithiation/delithiation process as previous reported.

$$xLi^+ + TiP_2O_7 + xe \rightarrow Li_x\left(Ti^{3+}_x Ti^{4+}_{1-x}\right)P_2O_7 \qquad (x \leq 1) \qquad \text{eq (1)}$$

$$Li_x\left(Ti^{3+}_x Ti^{4+}_{1-x}\right)P_2O_7 \rightarrow xLi^+ + TiP_2O_7 + xe \qquad (x \leq 1) \qquad \text{eq (2)}$$

Additionally, $Co_2P_2O_7$ and $Ni_2P_2O_7$ discharge/charge plots display in Fig. S18b and Fig. S18c with low coulombic efficiency in 1st cycle, which originates from reverse reaction in eq (3). For both materials in first cycle, voltage platform approximates to ~1.000 V (discharging) and ~1.800 V (charging) in Fig. S18b and Fig. S18c. The curve maintains stable with a compact discharge/charge plots in 2nd and 3rd cycles. Correspondingly, as pointed in CV curves (Fig. S18f and Fig. S18g), anodic peaks of two materials specifically appear in voltage of 0.897 V / 1.174 V at first cycles, attributing to irreversible reaction of simple substance Co/Ni formation in eq (3) respectively. This peak shifts to 1.559 V ($Co_2P_2O_7$) and 1.376 V ($Ni_2P_2O_7$) in 2nd and 3rd cycles, while reversible reaction is positioned at 1.683 V for $Co_2P_2O_7$ (Fig. S18f) and 1.841 V for $Ni_2P_2O_7$ (Fig. S18g) in three cycles, corresponding with eq (4).

$$M_2P_2O_7 + 2Li^+ + 2e^- \rightarrow Li_2MP_2O_7 + M \qquad (M=Ni, Co) \qquad \text{eq (3)}$$

$$Li_2MP_2O_7 + 2Li^+ + 2e^- \leftrightarrow Li_4P_2O_7 + M \qquad (M=Ni, Co) \qquad \text{eq (4)}$$

Besides, we imprimis investigate electrochemical performance of $Fe_2Fe(P_2O_7)_2$ material. Here we assume the electrochemical reaction about $Fe_2Fe(P_2O_7)_2$ material in Seq (1~5) (support information) with irreversible part and reversible part. There

displays slight peak pointed with star in Fig. S18h, which might be attributing to reduction of Fe^{3+} to Fe^{2+} in Seq (1). Its discharge/charge properties are displayed in Fig. S18d. First cycle shows discharge capacity for 1062.8 mA h g^{-1} and charge capacity of 793.8 mA h g^{-1}in 0.1 A g^{-1}, attributing to irreversible conversion of $Fe_{(ir)}$ in Seq (2). When lithium ion inserts into the $Fe_2Fe(P_2O_7)_2$ material in the first discharge process, it obviously observed that irreversible peak in 0.569 V appears in first cycle, which might be inducing irreversible conversion of Fe^{2+} into one Fe(ir). Additionally, CV curve shows first anodic peak in 0.569 V for first cycles and peak shifts to 1.547 V for 2nd and 3rd cycles in Fig. S18h, which is according with this. It might be induced by formation of SEI membrane and irreversible reaction of phase transformation about Fe shown in Seq (2). First charge curve presents two platforms around 1.683 V ($Fe \rightarrow Fe^{2+}$) and 2.325 V ($Fe^{2+} \rightarrow Fe^{3+}$) for charge cycles relating to reaction in Seq (3) and Seq (4). It conjectures that the electrochemical process maintains as a circle between Seq (3-4) in charge and Seq (5) in discharge.

As it shows in Fig. S18i, four types of pyrophosphate materials as obtained present electrochemical curve maintaining as almost a straight line in voltage of 0.01V-3.00 V with current rate of 1 A g^{-1} in 800 cycles. TiP_2O_7 delivers the 476.0 mA h g^{-1} reversible capacity after 800 cycles. Meanwhile, the $Co_2P_2O_7$ and $Ni_2P_2O_7$ are assigned to 441.7 mA h g^{-1}, 311.3 mA h g^{-1} reversible capacity indexing excellent electrochemical performance. Simultaneously, $Fe_2Fe(P_2O_7)_2$ material delivers the 423.4 mA h g^{-1} under 800 cycles. All the materials deliver more than 91% capacity retention rate, suggesting stable electrochemical performance of MP_2O_7 (M=Ti, Co, Ni, Fe).

Seq (5-11)

$$Mn_2P_2O_7 + 2Na^+ + 2e^- \rightarrow Na_2MnP_2O_7 + Mn \quad (5)$$
$$Na_2MnP_2O_7 + 2Li^+ + 2e^- \leftrightarrow Na_4P_2O_7 + Mn \quad (6)$$
$$Mn + xNa^+ + 2e^- \leftrightarrow Na_xMn \quad (7)$$

$$Mn_2P_2O_7 + 2Na^+ + 2e^- \rightarrow Na_2MnP_2O_7 + Mn \quad (8)$$
$$Na_2MnP_2O_7 + 2Li^+ + 2e^- \leftrightarrow Na_4P_2O_7 + Mn \quad (9)$$
$$Mn + xK^+ + 2e^- \leftrightarrow K_xMn \quad (10)$$
$$C + xK^+ + xe^- \leftrightarrow K_xC \quad (11)$$

Table S1. D parameters details calculated by CV testing of MPO and MPO-rGO.

sample	Charge D_{Li^+} (cm^2 S^{-1})	Discharge D_{Li^+} cm^2 S^{-1}
MPO	3.51×10^{-3}	1.29×10^{-2}
MPO-rGO	8.17×10^{-3}	1.46×10^{-2}

Table S2. Lithium ion diffusion and EIS statistic of EIS.

Sample	Cycles	σ	Rsf	Rct	D_{Li^+} (cm^2 S^{-1})
MPO	1st	73.364	9.448	50.990	3.75×10^{-12}
	2nd	192.269	5.536	98.340	1.43×10^{-13}
	3rd	183.292	5.347	91.64	1.50×10^{-13}
	4th	185.183	5.096	90.800	1.48×10^{-13}
	5th	190.185	5.223	92.46	1.44×10^{-13}
	6th	183.517	5.232	91.54	1.50×10^{-13}
MPO-rGO	1st	26.368	3.976	58.400	1.04×10^{-13}
	2nd	84.570	5.569	169.5000	3.25×10^{-12}
	3rd	85.109	5.689	175.200	3.23×10^{-12}
	4th	89.729	4.781	203.300	3.06×10^{-12}
	5th	92.298	5.222	208.100	2.98×10^{-12}
	6th	91.875	7.115	220.000	2.99×10^{-12}

$Z^{'} = R_{sf} + R_{ct} + \sigma\omega^{-1/2}$